Earth and Planetary Science Letters 361 (2013) 272–286

Contents lists available at SciVerse ScienceDirect

Earth and Planetary Science Letters

journal homepage: www.elsevier.com/locate/epsl

Spatial distribution of volcanoes on Io: Implications for tidal heating and magma ascent

Christopher W. Hamilton [a,*], Ciarán D. Beggan [b], Susanne Still [c], Mikael Beuthe [d], Rosaly M.C. Lopes [e], David A. Williams [f], Jani Radebaugh [g], William Wright [c]

[a] Planetary Geodynamics Laboratory, NASA Goddard Space Flight Center, Greenbelt, MD, USA
[b] British Geological Survey, Edinburgh, UK
[c] Information and Computer Sciences, University of Hawaii at Mānoa, Honolulu, HI, USA
[d] Royal Observatory of Belgium, Brussels, Belgium
[e] Jet Propulsion Laboratory, California Institute of Technology, Pasadena, CA, USA
[f] School of Earth and Space Exploration, Arizona State University, Tempe, AZ, USA
[g] Geological Sciences, Brigham Young University, Provo, UT, USA

ARTICLE INFO

Article history:
Received 26 September 2011
Received in revised form
10 October 2012
Accepted 13 October 2012
Editor: T. Spohn
Available online 11 December 2012

Keywords:
volcanism
hotspots
paterae
spatial distribution
tidal dissipation
Io

ABSTRACT

Extreme volcanism on Io results from tidal heating, but its tidal dissipation mechanisms and magma ascent processes are poorly constrained. Here we analyze the distribution of volcanic hotspots and paterae identified within the first 1:15,000,000-scale global geologic map of Io to characterize their patterns of spatial organization. Ionian hotspots correspond to the locations of positive thermal anomalies that have been detected since 1979, whereas paterae are caldera-like volcano-tectonic depressions that record locations of volcanic activity over a longer period of geologic time (up to ~1 million years). Some (~20%) of patera floor units are associated with active hotspots, but the majority appeared to be extinct or dormant at the time of observation. Volcano distributions are useful for testing interior models of Io because the relative strength of tidal heating in the asthenosphere and deep-mantle greatly affect expected patterns of surface heat flux. We examine the spatial distribution of volcanic centers using nearest neighbor (NN) statistics and distance-based clustering. Nearest neighbor analysis reveals that hotspots (i.e., sites of active volcanism) are globally random, but closer to the equator, they are uniform (i.e., more widely spaced than a random model would predict). This suggests that magma scavenging around active volcanic systems in the near-equatorial region may drive hotspots apart, whereas vigorous mantle convection and/or deep-mantle heating may reduce surface heat flux variations and promote spatial randomness on a global scale. In contrast to the hotspots, NN patera floor units tend to be clustered, which implies that multiple eruptive units tend to form in association with most volcanic systems. Generalized paterae, which represent volcanic systems, tend to be uniformly distributed, except in the northern regions, where their distribution is random. This implies that most volcanic systems interact with one another and repel, except at high northern latitudes, where they appear to form independently. Distance-based clustering results support a dominant role for asthenospheric heating within Io, but show a 30–60° eastward offset in volcano concentrations from predicted locations of maximum surface heat flux along the tidal axis. This offset may imply faster than synchronous rotation, a role for lateral advection of magma within Io's interior prior to its eruption, state of stress controls on the locations of magma ascent, and/or a missing component in existing tidal dissipation models, such as the effects of fluid tides generated within a globally extensive layer of interconnected partial melt.

1. Introduction

Io, the innermost of Jupiter's Galilean satellites, is the most volcanically active body in the Solar System (McEwen et al., 1998, 2000a, 2000b; Lopes-Gautier et al., 1999; Spencer et al., 2000). Io's global mean heat flow is not precisely known, but estimates generally range from 1.5 to 4.0 W m^{-2} (Moore et al., 2007), with the most recent astrometric observations supporting a value of 2.24 ± 0.45 W m^{-2} (Lainey et al., 2009). This mean surface heat flux is ~20 times larger than the Earth's (Turcotte and Schubert, 2002), but unlike the Earth, Io's internal heat comes primarily from the dissipation of tidal energy and not from radiogenic sources (Peale et al., 1979; Moore et al., 2007). Io's Laplace resonance with Europa

* Correspondence to: Planetary Geodynamics Laboratory, NASA Goddard Space Flight Center, Mail Code 698, Greenbelt, MD 20771, USA. Tel.: +1 301 305 3818 (Mobile), +1 301 614 6749 (Office).
E-mail address: christopher.hamilton@nasa.gov (C.W. Hamilton).

0012-821X/$ - see front matter © 2012 Elsevier B.V. All rights reserved.
http://dx.doi.org/10.1016/j.epsl.2012.10.032

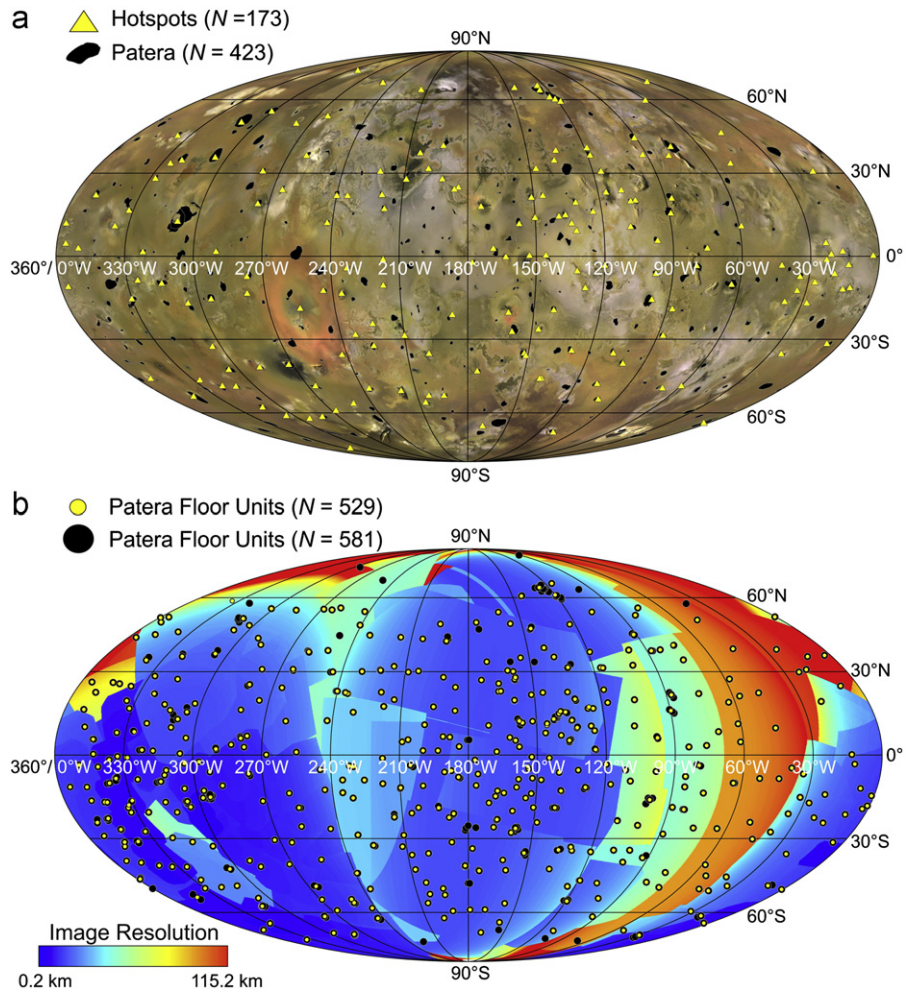

Fig. 1. Mollweide projections of the global distribution of volcanoes on Io. (a) Hotspots (N=173) and caldera-like paterae (N=423) overlaid on a *Galileo-Voyager* image mosaics reprocessed to a spatial resolution of 1 km/pixel (Becker and Geissler, 2005). (b) Centroids of patera floor units from Williams et al. (2011a) N=529, and Williams et al. (2011b) N=581, overlaid on a map showing the variability of the best imagery used to make the *Galileo-Voyager* basemap. The color bar has a linear stretch between 0 and 116 km, with a range of resolutions spanning from 0.2 km to 115.2 km. In this study, all coordinates are west positive, measured from a prime meridian crossing through the subjovian point of Io.

and Ganymede maintains all three satellites in noncircular orbits, which results in continuous deformation and frictional heating of the satellite's interior (e.g., Peale et al., 1979; Ross and Schubert, 1985; Ross et al., 1990; Schubert et al., 1986; Segatz et al., 1988; Tackley, 2001; Tackley et al., 2001; Moore et al., 2007). Heat produced within Io's interior is predominantly advected to the surface by ascending silicate magma and not conducted through its lithosphere (McEwen et al., 2004). The heat-pipe mechanism proposed for transporting Io's internal thermal energy to the surface (O'Reilly and Davies, 1981) involves bringing magma upward through "hotspots" that are embedded within a relatively cold lithosphere. Analysis of Io's global distribution of volcanoes (Fig. 1) can therefore provide information about the moon's internal structure, thermo-rheological properties, tidal dissipation mechanisms, processes of melt generation, and magma transport. Better understanding these processes for Io also provides insight into similar tidal heating mechanisms operating on other worlds, such as Europa and Enceladus, as well as tidally-heated exoplanets.

2. Io's internal structure and its relation to tidal dissipation models

The *Galileo* mission revealed that Io is a differentiated body consisting of a metallic iron core, with a radius of 650–950 km, surrounded by a silicate mantle (Moore et al., 2007). The thickness and composition of the crust are unknown, but must contribute to a strong lithosphere that is capable of supporting the elastic stresses that are associated with mountains up to ~18 km in height (Schenk et al., 2001; Jaeger et al., 2003). The structure and temperature distribution within the mantle are debated, but Keszthelyi et al. (2007) suggest a potential temperature between 1523 and 1723 K, with a preferred value of ~1573 K. They also claim that the top of the mantle is likely partially molten, with 20–30 vol% rock melt. The presence of a global layer with ≥20% interconnected partial melt and >50 km thickness (i.e., the proposed asthenosphere) is consistent with *Galileo* magnetometer data of Io's induced magnetic field (Khurana et al., 2011).

In end-member tidal dissipation models, the bulk of Io's heating occurs either within the deep-mantle or within the asthenosphere (Ross and Schubert, 1985; Schubert et al., 1986; Segatz et al., 1988; Tackley et al., 2001), while in mixed models heating is partitioned between these end-members (Ross et al., 1990; Tackley et al., 2001). Computations of heat production usually assume a spherically symmetric interior (for a 3D approach see Běhounková et al., 2010) having a linear viscoelastic rheology of the Maxwell type. In the simplest approximation, heat is transferred radially to the surface by an unspecified mechanism, but in more realistic models, heat is transported either by

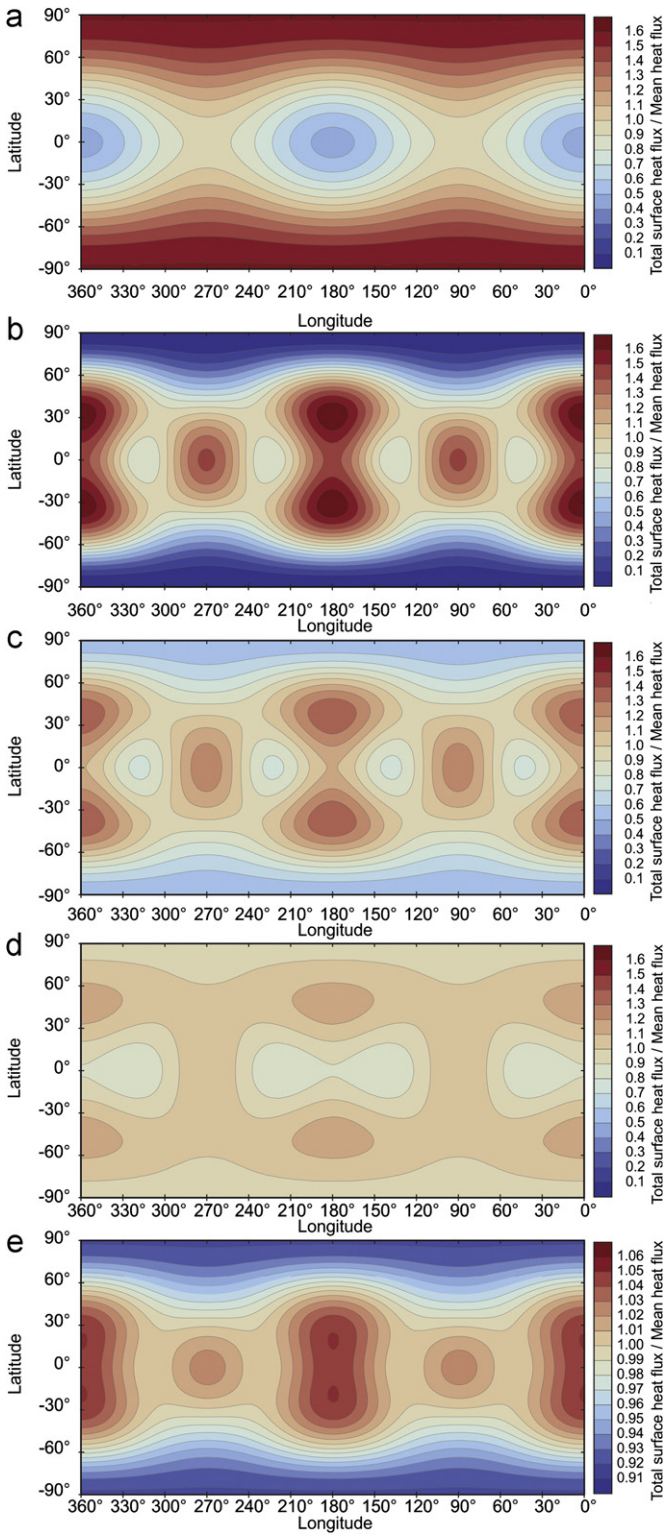

Fig. 2. Patterns of surface heat flux due to tidal dissipation for various interior models. (a) Deep-mantle heating end-member. (b) Asthenospheric-heating end-member. (c) Linear combination of end-member models, with the deep-mantle and asthenosphere producing 1/3rd and 2/3rd of the heat, respectively. (d) Minimum surface heat flux variation model ($<20\%$ variation) generated by a combination of 61% deep-mantle and 39% asthenospheric heating. (e) Asthenospheric end-member heating pattern averaged by lateral flows due to convection (n.b., change of scale in (e) relative to (a–d)). See Section 2 for model parameters.

convective flow (Tackley et al., 2001) or by melt segregation (Moore, 2001). In deep-mantle heating models (Fig. 2a), the surface heat flux is maximum near the poles and minimum at the equator, with absolute minima occurring at the subjovian (0°N, 0°W) and antijovian points (0°N, 180°W). In asthenospheric models, heat flux is minimum at the poles and maximum in the equatorial area, with primary maxima occurring north and south of the subjovian and antijovian points (at approximately $\pm 30°$ latitude), and with secondary maxima occurring at the centers of the leading (0°N, 90°W) and trailing (0°N, 270°W) hemispheres (Fig. 2b). Spatial variations in surface heat flux are lower in mixed models, with maxima progressively migrating toward the poles as deep-mantle heating is added to the asthenospheric heating component (Fig. 2c and d). Moderate convection does not fundamentally change these patterns, but as convection becomes more vigorous (i.e., for increasingly large Rayleigh numbers), horizontal flows will smooth out lateral heat flux variations. The amplitude of surface heat variations decreases in inverse proportion to their wavelength (Tackley, 2001) and ultimately disappear if the Rayleigh number becomes very large. The deep-mantle heating pattern is nearly pure harmonic degree 2 and therefore convection uniformly reduces the amplitude of surface heat flux variations due to dissipation in the mantle. By contrast, the strong degree 4 harmonic component in the asthenospheric pattern is reduced more greatly by lateral flows than the degree 2 component, and so the resulting structure shows more heat concentration near the equator, particularly close to the subjovian and antijovian points (Fig. 2e).

Surface heat flux patterns in Fig. 2 are computed with spherically symmetric interior models having three or four homogeneous incompressible layers (Segatz et al., 1988; Spohn, 1997). All models have a fluid core, a viscoelastic mantle with a Maxwell rheology and a thin elastic lithosphere or crust. In asthenospheric models, the mantle is subdivided into a high-viscosity deep-mantle and a low-viscosity asthenosphere. The core radius, core density, mantle density, and lithospheric thickness are chosen to be 980 km, 5150 kg/m^3, 3200 kg/m^3 and 30 km, respectively, as in Segatz et al. (1988). These parameters represent only one example of a possible interior structure of Io (see Moore et al., 2007; Turtle et al., 2007, for alternative examples), but these choices are not crucial for the computation of dissipation patterns. The most important factor is the rheology of the mantle and specifically the presence (or absence) of an asthenosphere. The thickness of the asthenosphere (if present) is set to 50 km, which is the lower bound for the global magma layer discussed in Khurana et al. (2011). We solve the equations for displacement, stress, and gravitational perturbation with the propagator matrix technique (e.g., Sabadini and Vermeersen, 2004; Roberts and Nimmo, 2008) and compute the dissipation rate per unit volume by summing on the squared strains (Peale and Cassen, 1978; Segatz et al., 1988; Tobie et al., 2005). The surface heat flux is computed with the assumption that the heat flows radially to the surface. The unknown shear modulus μ and viscosity η of the lithosphere are set to $\mu = 65 \times 10^9$ Pa and $\eta = 10^{23}$ Pa s, and for the deep-mantle they are $\mu = 60 \times 10^9$ Pa and $\eta = 10^{20}$ Pa s, as in Segatz et al. (1988). The shear modulus and viscosity of the upper-mantle and asthenosphere are chosen in order to generate the correct total power of about 10^{14} W (Moore et al., 2007). In the deep-mantle end-member heating model (Fig. 2a), the upper-mantle has $\mu = 3.5 \times 10^9$ Pa and $\eta = 10^{15}$ Pa s. In the asthenospheric end-member model (Fig. 2b), the asthenosphere has $\mu = 4 \times 10^4$ Pa and $\eta = 10^{10}$ Pa s. Fig. 2c shows a mixed model with a linear combination of 1/3rd deep-mantle and 2/3rd asthenospheric heating. The model with minimum variance of the surface heat flux (Fig. 2d) was generated by a mixture of 61% deep-mantle ($\mu = 3.5 \times 10^9$ Pa, $\eta = 4.7 \times 10^{14}$ Pa s) and 39% asthenospheric ($\mu = 3 \times 10^4$ Pa, $\eta = 10^{10}$ Pa s) heating. The given values of shear modulus and viscosity are one possible choice among many generating the same total heat flux (e.g., Spohn, 1997)

and have not been determined from a realistic mineralogical composition of Io. The effect of lateral flows on the asthenospheric pattern (Fig. 2e) is approximated with the scaling law for boundary-focused heating (Eq. 11 of Tackley, 2001). For our asthenospheric model, the Rayleigh number for internal heating is 7.2×10^{13} (see Eq. 5 of Tackley, 2001), with the heat capacity, thermal diffusivity and thermal expansivity as in Table 1 of Tackley (2001). The non-zero harmonic components of the heat flux are reduced by factors of 9.6 (degree 2, aspect ratio ~60) and 19.2 (degree 4, aspect ratio ~30), with the aspect ratio being the ratio of the half-wavelength of the spatial pattern to the depth (here 50 km) of the asthenosphere (Tackley, 2001).

If the assumption that volcanic centers are directly correlated with surface heat flux is correct, then the spatial distribution of volcanoes on Io may be used to distinguish between these tidal dissipation models. Previous studies (e.g., Carr et al., 1998; McEwen et al., 1998, 2000b; Lopes-Gautier, 1999), suggested that the global distribution of volcanic centers on Io appears "uniform", by which they mean homogeneously distributed over the moon's surface, but not necessarily spaced at regular intervals. However, they also noted greater concentrations of volcanoes at low latitudes. This result is consistent with tidal dissipation occurring more in the asthenosphere than the deep-mantle (Lopes-Gautier, 1999). Others have shown that volcanic centers (some of which are active hotspots) are clustered within several tens of degrees of the subjovian or antijovian points (e.g., Radebaugh et al., 2001; Schenk et al., 2001; Tackley et al., 2001; Veeder et al., 2011, 2012). Kirchoff et al. (2011) also identified a dominant degree 2 clustering pattern among volcanic centers using spherical harmonic analysis, but they note that the higher degrees of the power spectrum are consistent with randomness and even repelling (i.e., greater than random spacing). To explore the significance of these contrasting observations, we reexamine the spatial distribution of hotspots and paterae on Io at multiple scales using several statistical techniques and insights from new global geologic maps of Io (Williams et al., 2011a, 2011b).

3. Inventory of hotspots and paterae on Io

Volcanic centers on Io include hotspots and paterae that have been identified using spacecraft images and Earth-based telescopes. Ionian hotspots are positive thermal anomalies associated with sites of active volcanism, whereas paterae are caldera-like volcano-tectonic depressions (described below) that may, or may not, be currently active. Approximately two-thirds of the 173 hotspots are located within patera floor units, which implies ~20% of the 529 patera floor units (Williams et al., 2011a) were volcanically active at the time of observation. Additional patera floor units may be also active, but their thermal anomalies have not been resolved to date given temporal, spatial, and other thermal remote sensing constraints. Hotspots located outside patera structures may either represent primary volcanic systems lacking a well-developed caldera-like feature, or be associated lava flows that have transported hot material away from their source through thermally insulated internal pathways (e.g., lava tubes). Hotspot observations therefore provide a statistical sample of the locations where active volcanic processes have occurred on Io since their initial discovery in 1979 (Smith et al., 1979a, 1979b). In contrast, paterae represent a longer window into Io's volcanic history, spanning up to ~1 million years (i.e., Io's timescale of resurfacing; McEwen et al., 2000a, 2004).

The hotspot database used in this study (Fig. 1a) comprises all thermal anomalies presented in Table A.1 of Lopes and Spencer (2007), plus the "East Girru" hotspot (22°N, 235°W) identified by *New Horizons* (Spencer et al., 2007). The database also includes Ra Patera (8.3°S, 325.2°W). Ra Patera lacks an observed positive thermal anomaly, but it is included in our database as hotspot because its activity was confirmed by the detection of an associated volcanic plume (Lopes et al., 2004).

Paterae on Io are generally interpreted to be morphologically analogous to terrestrial calderas (Carr et al., 1998; Radebaugh et al., 2001; McEwen et al., 2004). Paterae have a wide range of shapes, ranging from circular to irregular, with irregular paterae thought to have formed under the influence of structural or tectonic controls (for a complete overview see Radebaugh et al., 2001). Patera floors show a wide range of complexity, depending upon the spatial resolution of the images. At high resolution, patera floor units contain a mixture of relatively bright and dark features, irregular hummocks, and pits (e.g., Chaac Patera; Williams et al., 2002). At lower resolution, patera floors range from dark gray to black to bright pinkish-white to red–orange in color, with considerable variation in monochromatic albedo, color, and texture (Williams et al., 2011a, 2011b). Dark patera floor units often correlate with *Galileo* Near Infrared Mapping Spectrometer (NIMS) and Photopolarimeter-Radiometer (PPR) hotspots. Bright patera floor units tend not correlate with hotspots and NIMS data indicate an enhanced signature of sulfur dioxide in the white to pinkish-white material on several patera floors. These observations suggest that bright patera floor units exhibit colder temperatures and are inactive (Lopes et al., 2004). Based on morphological and mapping studies, Io's patera floor units are interpreted to be composed of lava flows, lava ponds, or lava lakes, in which darker units are thought to be silicate in composition, whereas brighter flows are either sulfur-rich materials or cold silicates covered by a mantle of sulfur-rich plume deposits and/or SO_2 frosts (Keszthelyi et al., 2001; Radebaugh et al., 2001; Turtle et al, 2004; Williams et al., 2007, 2011a, 2011b).

In the first complete 1:15,000,000-scale global geologic map of Io (Williams et al., 2011a, 2011b), patera floor units were mapped as bright, dark, and undivided, with some paterae being completely filled by a single floor unit, while others exhibit multiple units. The map was produced in ArcGIS using a set of combined *Galileo-Voyager* image mosaics reprocessed to a spatial resolution of 1 km/pixel (Becker and Geissler, 2005). There is some discrepancy between different workers on the number of paterae on Io (e.g., Radebaugh et al., 2001, Veeder et al., 2011, 2012; Williams et al., 2011a, 2011b), based on the different approaches used to define and identify them. In this study, we focus on the 529 patera floor units mapped by (Williams et al., 2011a; Fig. 1b), but also consider a modified distribution of 581 patera floor units presented by Williams et al. (2011b; Fig. 1b). The latter database includes very small paterae (< 20 km diameter) that were identified and mapped in the digital images, but were too small to appear on the published map sheet. In addition to these databases, we generalized the 581 patera floor units into 423 paterae that are intended to represent the locations of volcanic systems (Fig. 1a). These patera locations were obtained in ArcGIS by calculating the centroids of amalgamated patera floor units that are confined within topographic depressions. Coordinates for all hotspots (N=173), patera floor units (N=529 and 581) and paterae (N=423) are provided as Supplementary material.

Although global geologic maps of Io (Williams et al., 2011a, 2011b) are based on 1 km/pixel *Galileo-Voyager* mosaics, the resolution of the original image data was spatially variable, which raises the possibility of observational bias in the identification of volcanic centers. Fig. 1b and 3 illustrate the spatial variations in image resolution and suggests that poor quality data poleward of 60°N and 75°S and in the zone from 0°W to 90°W may have limited the detection of the smallest paterae in the extreme polar regions and in the subjovian and leading hemispheres. Nonetheless, 83% of Io's surface has been imaged at better than 5 km/pixel, with only 3% imaged at resolutions less than 10 km/pixel (Fig. 1b), and so given

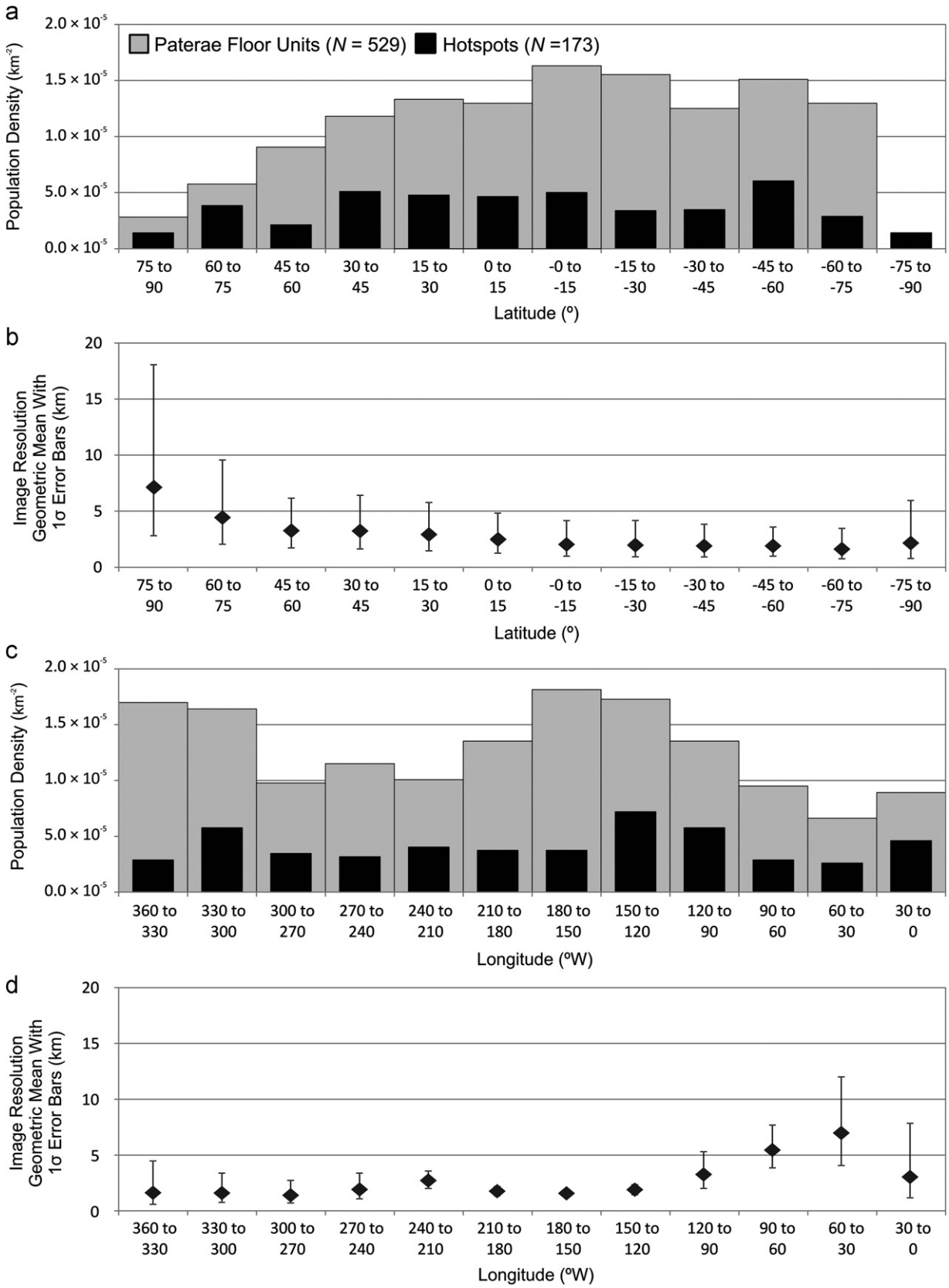

Fig. 3. Spatial variability in volcano distributions hotspots ($N=173$) and patera floor units ($N=529$). (a) Frequency distribution of volcanic centers as a function of latitude. (b) Geometric mean resolution with 1σ error bars plotted for each latitude bin. (c) Frequency distribution of volcanic centers as a function of longitude. (d) Geometric mean resolution with 1σ error bars plotted for each longitude bin.

that the mean diameter of the patera floor units ($N=529$) is 41.6 ± 27.6 km (at 1σ), the currently resolved volcanoes distributions are expected to provide a representative sample of the global distribution.

4. Methods

4.1. Nearest neighbor tests for randomness, uniformity, and clustering

To quantitatively characterize the distribution of volcanoes on Io, we developed new geospatial analysis tools to investigate the spatial relationship between points of interest on spherical bodies using nearest neighbor (NN) distance statistics. These tools are incorporated into a MATLAB package called Geologic Image Analysis Software (GIAS Version 2.0), which is freely available from www.geoanalysis.org. Pairwise distance relationships between nearest NN volcanic centers (i.e., hotspots, patera floor units, and paterae) are used to test for statistically significant departures from randomness. Our NN analyses utilize great-circle distances between volcanic centers, accounting for sample-size-dependent calculation biases in NN test statistics (Baloga et al., 2007; Beggan and Hamilton, 2010; Hamilton et al., 2010, 2011). In addition, we consider biases in NN test statistics introduced by analyzing on the surface of a sphere rather than a flat planar region (first recognized as an issue for NN analyses within this study).

The test statistic R is the ratio of the actual mean of the measured pairwise NN distances $\overline{r_a}$ compared to the expected mean of the pairwise NN distances $\overline{r_e}$ for a given population of sample-size N within region of interest of area A (Clark and Evans, 1954),

$$R = \frac{\overline{r_a}}{\overline{r_e}}. \tag{1}$$

Based on R, a test distribution could be consistent with the expected distribution model, clustered with respect to the model, or more uniform. A second statistic, c, evaluates the significance of the result implied by R (Clark and Evans, 1954),

$$c = \frac{\overline{r_a} - \overline{r_e}}{\sigma_e}, \tag{2}$$

where σ_e is the expected standard deviation based on a Poisson random distribution with N points within an area A.

$$\sigma_e = \frac{0.26136}{\sqrt{N^2/A}}. \tag{3}$$

Ideal values of R, c, and their standard deviations vary depending on the number of points N within the distribution and the shape of the region of interest (Fig. 4). Consequently, 1 and 2σ confidence limits are calculated for each test statistic and the significance of R and c are evaluated by taking into account N and the geometry of the region of interest.

The relative values of R and c allow us to make inferences about the nature of the spatial distribution of the points within the region of interest. If the departure of R from its ideal value is more negative than -2σ, the points are clustered relative to the null hypothesis, whereas if the departure of R is greater than $+2\sigma$ they tend toward spatial uniformity. If R and c are both outside their respective $\pm 2\sigma$ limits, then the input distribution exhibits a statistically significant departure from the null hypothesis,

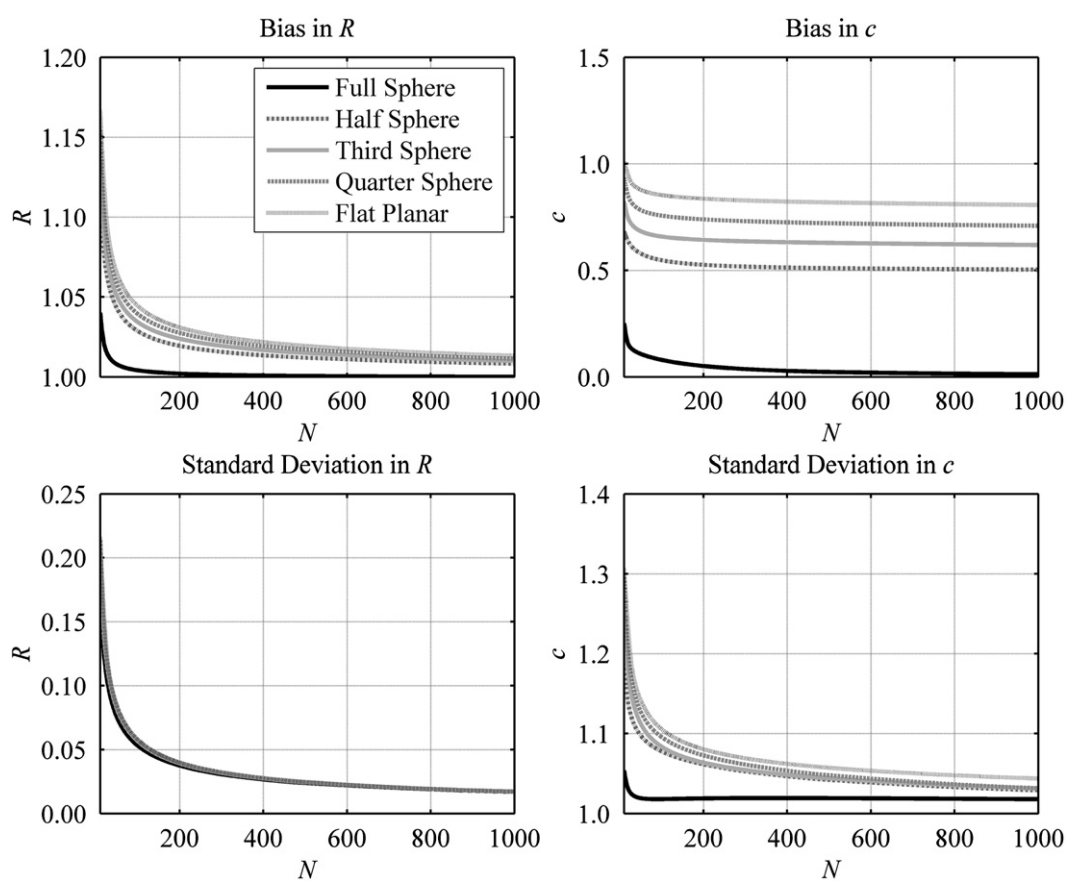

Fig. 4. Biases in nearest neighbor (NN) statistics. Bias in expected values of R, c, and their standard deviations computed from Monte-Carlo simulations of N randomly distributed points located on spherical to planar surfaces.

whereas if R and c are both within their $\pm 2\sigma$ limits, the null hypothesis cannot be rejected. If R is within its $\pm 2\sigma$ limits, while c is outside of them, or vice versa, then the results of the NN analysis would be inconclusive because the variance of the data is too large. In this study, the null hypothesis is a homogeneous Poisson model (i.e., spatial randomness).

Spatial patterns matching the null hypothesis should ideally have $R=1$ with $c=0$ (Clark and Evans, 1954). However, Baloga et al. (2007) noticed a significant bias away from the ideal values for R and c in their calculations for low N (<100). Using multiple Monte-Carlo simulations of the Poisson random distributions of N points, they computed a sample-size-dependent correction for the expected values of R and c and their standard deviations on a bounded planar surface. However, on an approximately spherical body, the biases are different because the surface has no boundaries. Hence when examining the global distribution of volcanoes on Io, we compute the correction for R and c using a Monte-Carlo simulation on a sphere rather than a flat plane. To construct random spatial distributions on a unit sphere, we generated N latitude (θ) and longitude (φ) pairs using the uniform distribution to compute positions $\theta=\sin^{-1}(2U(N)-1)$; $\varphi=2\pi U(N)$, where the uniform random variable $U(N)\in(0,1)$. The pairwise angular distances between these points approximates a Poisson distribution. To determine the effects of region of interest geometry and N, we divide the unit sphere into different regions (e.g., full sphere, hemisphere, etc.) and perform 4000 Monte Carlo simulations for N ranging from 10 to 1000 to obtain ideal values of R and c, and their standard deviations (Fig. 4). Second order exponential curves are fitted through these results for interpolation and plotting purposes. On a full sphere, NN statistics for the expected homogeneous Poisson distributions approach the theoretical values predicted by Clark and Evans (1954), whereas for smaller and increasingly closed areas (e.g., a half, third, and quarter of a sphere) the biases in R and c increase and approach the values for planar (i.e., Euclidean) geometries specified by Baloga et al. (2007). For Io, all angular distances are scaled to great-circle distances by multiplying them by the moon's mean radius (i.e., 1821.46 km, based on the standard "Io_2000" projection in ArcGIS).

We analyze volcano centers on Io in the following domains: global, northern hemisphere, southern hemisphere, subjovian hemisphere, antijovian hemisphere, leading hemisphere, trailing hemisphere, north polar, south polar, and near-equatorial. Polar and near-equatorial regions are specified by divisions at $\pm 19.47^\circ$ latitude to divide the surface area of Io into three equal thirds, thereby facilitating direct comparisons between these NN statistics. Dividing the surface area of Io into equal thirds at $\pm 19.47^\circ$ also minimizes the effects of potential resolution bias by considering large regions. For instance, zones of poor quality data poleward of 60°N and 75°S represent less than 20% and 5% of the total surface area in the north and south polar regions, respectively, and so we do not expect observational basis to significantly affect the statistical significance of our NN results.

4.2. Distance-based clustering

Nearest neighbor analysis considers pairwise distance relationships between objects, but does not reveal how those objects may be organized into larger groups. To identify larger regional groups among hotspots ($N=173$) and patera floor units ($N=529$), we partition these volcanic centers into k clusters using the distance-based clustering technique described below.

A solution that reveals two clusters ($k=2$) located at the north and south poles would indicate whole-mantle convection with plumes impinging on the poles (Fig. 2a) and generating enhanced volcanism at high latitudes. In contrast, two clusters located at low latitudes along the tidal axis (Fig. 2b) would indicate that heating and convection occurs mainly in the asthenosphere, with hot material rising and impinging on the base of the lithosphere at the subjovian and antijovian points and increasing volcanic activity in these regions (Tackley et al., 2001; Radebaugh et al., 2001). Significant tidal dissipation in the asthenosphere could also be inferred if volcanic centers concentrate into six clusters ($k=6$) that coincide with the locations of the six surface heat flux maxima predicted by asthenospheric-dominated tidal heating models (e.g., Fig. 2b and c). Recent spherical harmonic analysis of volcanic centers on Io (Kirchoff et al., 2011) lends support to focusing on clustering patterns that involve two and six groups because statistically significant clusters (beyond 2σ) were identified only at degrees 2 and 6.

In our distance-based clustering approach, we identify the locations of the k cluster centers that minimize the overall great-circle distance between all points (i.e., hotspots or patera floor units) and their nearest cluster center. This is achieved by iteratively (1) assigning points to clusters according to an optimization criterion, and then (2) computing the corresponding cluster center locations by averaging over the position of the points assigned to each cluster. This iteration is repeated until convergence. Algorithms of this kind (e.g., k-means clustering algorithms; Lloyd, 1957; Lillesand and Kiefer, 2000) are prone to finding local optima in an objective function, and so we use an optimization technique known as deterministic annealing (DA; Rose, 1998) to find the globally optimum solution. Each clustering solution is described by the assignments of N volcanic centers ($i=1,\ldots,N$), with geographical locations $\boldsymbol{x}_i$, to k cluster centers ($j=1,\ldots,k$), with locations $\boldsymbol{y}_j$. We consider probabilistic assignments given by the conditional probabilities $p(j|i)$ and the (conditional) entropy of these assignment probabilities is given by,

$$H=-\frac{1}{N}\sum_{j=1}^{k}\sum_{i=1}^{N}p(j|i)\ln[p(j|i)]. \tag{4}$$

Overall, the objective of the clustering problem is to find the solution that minimizes the average distance,

$$D=\frac{1}{N}\sum_{j=1}^{k}\sum_{i=1}^{N}p(j|i)d\left(\boldsymbol{x}_i,\boldsymbol{y}_j\right), \tag{5}$$

where $d(\boldsymbol{x}_i,\boldsymbol{y}_j)$ denotes great-circle distance obtained using the Haversine formula. To find the globally optimal solution we first find a maximum entropy model (Shannon, 1948; Jaynes, 1957; Rose, 1998) at a fixed value of D by solving the constrained optimization problem (Rose, 1998),

$$\min_{p(j|i)}(D-\lambda H), \tag{6}$$

$$\Leftrightarrow \min_{p(j|i)}\sum_{j=1}^{k}\sum_{i=1}^{N}p(j|i)\left(d\left(\boldsymbol{x}_i,\boldsymbol{y}_j\right)+\lambda\ln[p(j|i)]\right), \tag{7}$$

at a given value of λ. In the next step, we use DA to slowly move through a family of such models by gradually changing the trade-off parameter λ according to an annealing schedule, $\lambda\leftarrow\lambda/\alpha$, with $\alpha>1$. In the final solution, volcanic centers are assigned to the nearest cluster center using a deterministic assignment of either 1 or 0.

The optimization Eq. (7) has the formal solution,

$$p(j|i)=\frac{1}{Z(i,\lambda)}e^{-(1/\lambda)d(\boldsymbol{x}_i,\boldsymbol{y}_j)}, \tag{8}$$

where $Z=\sum_{j=1}^{k}e^{-(1/\lambda)d(\boldsymbol{x}_i,\boldsymbol{x}_j)}$ ensures normalization. The algorithm iteratively calculates the cluster memberships, Eq. (8), and the cluster center locations, which we determine as the mean location of the volcanic centers assigned to each cluster, weighted

by their cluster membership probability. Note that this is a simplification and that it deviates slightly from obtaining the cluster centers directly from the objective function, Eq. (7).

The DA algorithm is initialized by specifying k, annealing rate α, and a very large starting value for λ, which results in initial uniform assignments of the volcanic centers to each cluster. The algorithm then enters into two nested loops. The outer loop changes λ by dividing the previous λ by α, while the inner loop iteratively computes $p(j|i)$, $\boldsymbol{y}_j$, and $d(\boldsymbol{x}_i,\boldsymbol{y}_j)$, $\forall$ i, j. After convergence at the current value of λ, results are used as initial conditions for the next iterations of the algorithm at the new value of λ.

If the rate α at which λ is decreased is small enough then, as $\lambda \rightarrow 0$, the DA algorithm is guaranteed to find the data partition that corresponds to the global minimum of the average within cluster distances (Geman and Geman, 1984). Using this method we analyzed the global distributions of hotspots ($N=173$) and paterae ($N=529$) using $k=2$ and 6, with $\alpha=1.01$.

The DA algorithm is guaranteed to find the globally optimum solution, but any meaningful cluster analysis should be stable under sample fluctuations. Since we have only one dataset, we use random perturbations to the input data to estimate the uncertainty in the clustering solutions. Hotspot locations were perturbed in a random direction by a distance drawn from a Gaussian distribution set to the mean effective radius of the patera floor units ($N=529$), with an uncertainty of 1σ (i.e., 20.8 ± 13.8 km). Patera floor unit locations were perturbed in a random direction by their effective radius. For each of the four clustering scenarios, we created 1000 perturbed versions of the hotspot and patera floor unit databases, found the corresponding optimal solutions, and calculated the variance of the objective function value at the optimum. Next, we returned to the unperturbed datasets and accumulated 100,000 suboptimal solutions for each of the $k=2$ scenarios, and 30,000 for each of the $k=6$ scenarios. Suboptimal solutions were obtained by increasing the annealing rate α. For every solution, we calculated the average displacement between each suboptimal cluster center and the nearest optimal cluster center and identified the results with an average displacement within 1σ of the global optimum solution, based on the variance of the 1000 perturbed datasets for each scenario. The maximum average displacement among all of the identified suboptimal solutions provides a rough estimate of our uncertainty in the cluster center locations (see Supplementary Material for more detail).

In summary, our distance-based clustering approach uses an optimization technique known as deterministic annealing (DA) to find the optimal assignment of each volcanic center (i.e., hotspot or patera floor unit) to the nearest of k cluster centers. However, optimal solutions do not necessarily represent the only realistic fits to the data and so after determining the optimal partitioning of volcanic centers into k clusters, we estimate the uncertainty in the cluster center locations by considering the variations among suboptimal solutions. We have assumed equal weightings for each volcanic center, but to account for variable power output within (Rathbun et al., 2002) and between (Veeder et al., 2009, 2012) heat sources on Io, future geospatial analyses may be improved by weighting volcanic centers by their proportion of total power output.

5. Results

5.1. Nearest neighbor analyses

The global NN distribution of hotpots on Io is consistent with a homogeneous Poisson model, whereas the global distribution of patera floor units ($N=529$) is clustered relative to the null hypothesis (Table 1 and Fig. 5a and b). Hotspot NN distances are globally unimodal with a peak at 225–300 km (Fig. 6a), whereas the NN distances between patera floor units are bimodal with a primary mode at distances <75 km and a secondary mode between 150 and 225 km (Fig. 6a). To explore how sensitive these NN results are to the choice of paterae database, we also examined the patera floor units ($N=581$) from Williams et al. (2011b) and a database of paterae ($N=423$) that represent the locations of caldera-like depressions that are interpreted to be volcanic systems (see Section 3 and Fig. 1a). Table 1 and Fig. 5 summarize the results with more detailed data presented in Tables 5–8 of the Supplementary material section.

On a global scale, the $N=529$ and 581 patera floor unit distributions both show statistically significant clustering (beyond 2σ) relative to a homogeneous Poisson model (Fig. 5a and b). However, $N=581$ distribution has more patera floor units with NN distances <50 km (Fig. 6b), which accounts for the stronger tendency toward clustering. In contrast, the global distribution of paterae ($N=423$) exhibits statistically significant departures from the homogeneous Poisson model, with R and c exceeding their respective upper 2σ thresholds (see Supplementary material for more detail). This implies that paterae are self-organized into a repelled distribution with a greater than random average NN spacing. Differences in the NN statistics between the paterae ($N=423$) and patera floor units ($N=529$ and 581) are largely due to the occurrence of multiple patera floor units in association with most volcanic systems. This can been seen in the frequency distributions of the paterae and patera floor units (Fig. 6b) in that NN distances between paterae are unimodal with a peak between 150 and 225 km, while the patera floor units are bimodal with a sharp primary mode at distances <25 km and a broad secondary mode between approximately 125 and 200 km (i.e., similar to the modal spacing between paterae). The primary mode in patera floor unit NN

Table 1
Patterns of spatial organization implied by nearest neighbor (NN) analysis of volcanic centers on Io using 2σ thresholds in both R and c to mark statistically significant departures from the null hypothesis of a homogeneous Poisson (i.e., random) distribution.

	Hotspots ($N=423$)	Paterae ($N=423$)	Patera floor units ($N=529$)	Patera floor units ($N=581$)
Global	Random	Repelled	Clustered	Clustered
Northern Hemisphere (0–90°N)	Random	Random	Clustered	Clustered
Southern hemisphere (0–90°S)	Random	Repelled	Clustered	Clustered
Subjovian Hemisphere (270–90°W)	Random	Repelled	Clustered	Clustered
Antijovian Hemisphere (90–270°W)	Random	Repelled	Random	Clustered
Leading Hemisphere (0–180°W)	Random	Repelled	Clustered	Clustered
Trailing Hemisphere (180–0°W)	Random	Repelled	Clustered	Clustered
North Polar (19.47–90°N)	Random	Random	Clustered	Clustered
Near-Equatorial (19.47–19.47°S)	Repelled	Repelled	Random	Clustered
South Polar (19.47–90°S)	Random	Repelled	Clustered	Clustered

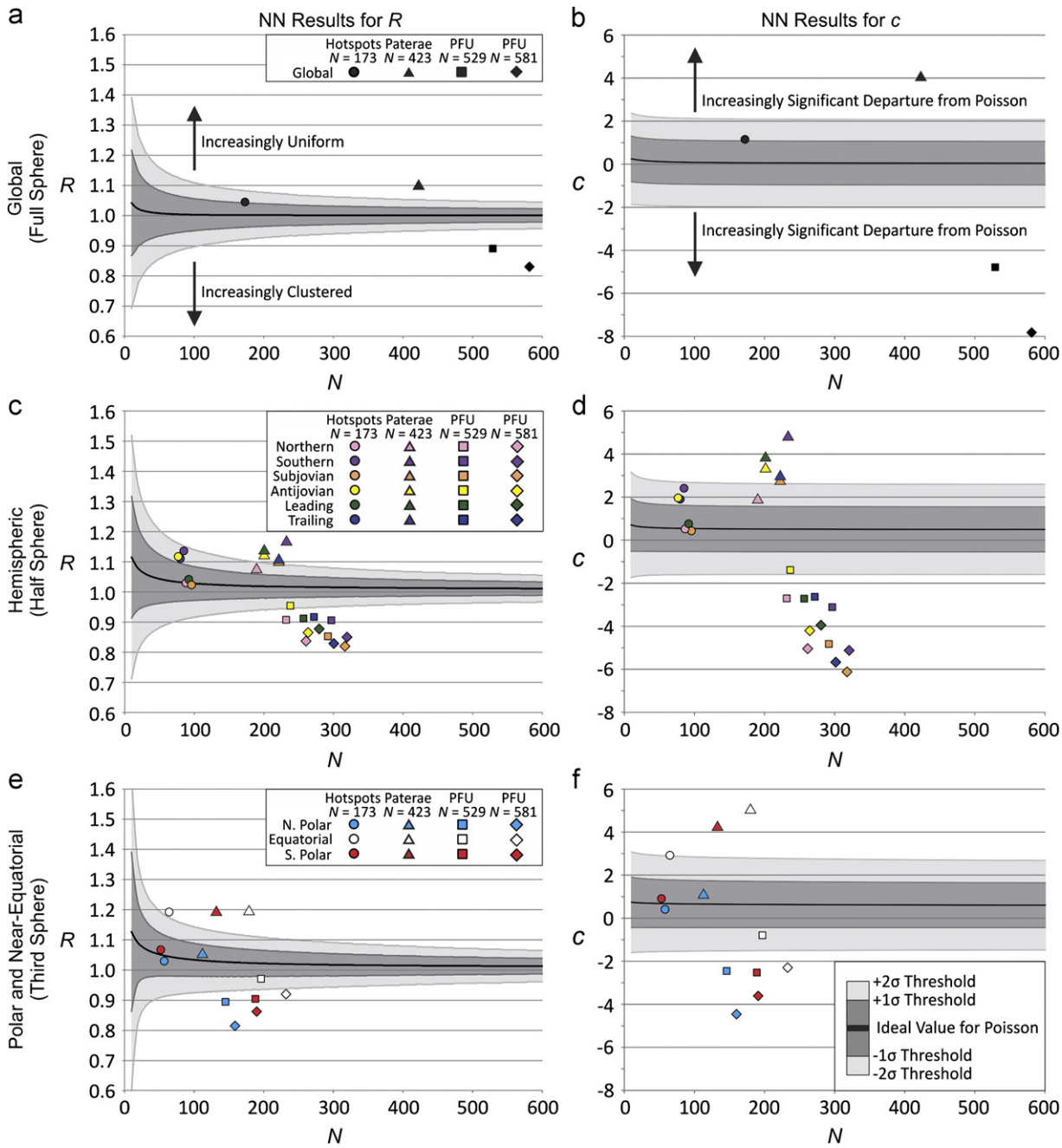

Fig. 5. Geodesic nearest neighbor (NN) results for hotspots (N=173), paterae (N=423), and patera floor units (PFU) distributions (N=529 and 581). Results for R (a, c, and e) and for c (b, d, and f). Ideal values for a homogeneous Poisson distribution are represented by black curves, with ± 1 and $\pm 2\sigma$ confidence limits identified by the upper and lower boundaries of the dark and light gray units, respectively. To identify statistically significant departures from randomness (i.e., reject the null hypothesis), both R and c must be outside their respective 2σ confidence limits. If R is above the upper 2σ limit, the distribution tends toward uniformity with NN pairs being repelled from one another, whereas if R is below the lower 2σ limit, the distribution tends toward clustering with NN pairs being more closely spaced than predicted by a homogeneous Poisson model. (a) and (b) Results for the global distribution of volcanic centers. (c) and (d) Results for each hemisphere. (e) and (f) Results for the near-equatorial and near-polar regions based $\pm 19.47^\circ$ latitude divisions.

frequency distribution may therefore reflect the spacing of erupted units within a volcanic system, whereas the secondary mode may indicate the spacing between neighboring volcanic systems.

Next we examine NN statistics for hotspots (N=173), patera floor units (N=529 and 581), and paterae (N=423) in each hemisphere. In all hemispheres, hotspot distributions are consistent with the homogeneous Poisson model (Fig. 5c and d), whereas patera floor units tend to be clustered. The only exception is the in antijovian hemisphere, using the N=529 database. In this case, NN distances exhibit a slight tendency toward clustering, but the departure from randomness is not significant at the 2σ level. For the paterae database (N=423), NN distances imply statistically significant repelling (i.e., a tendency toward uniformity) in all hemispheres except the northern hemisphere (Fig. 5c and d). In the northern hemisphere, paterae have R and c values between their respective upper 1 and 2σ bounds, which implies that the tendency toward uniformity in this region is not significant.

Lastly, divisions at $\pm 19.47^\circ$ latitude are used to compare the NN statistics of volcanic centers in the polar and near-equatorial regions of Io. Hotspots in the north and south polar regions are randomly distributed within 1σ limits of R and c (Fig. 3e and f),

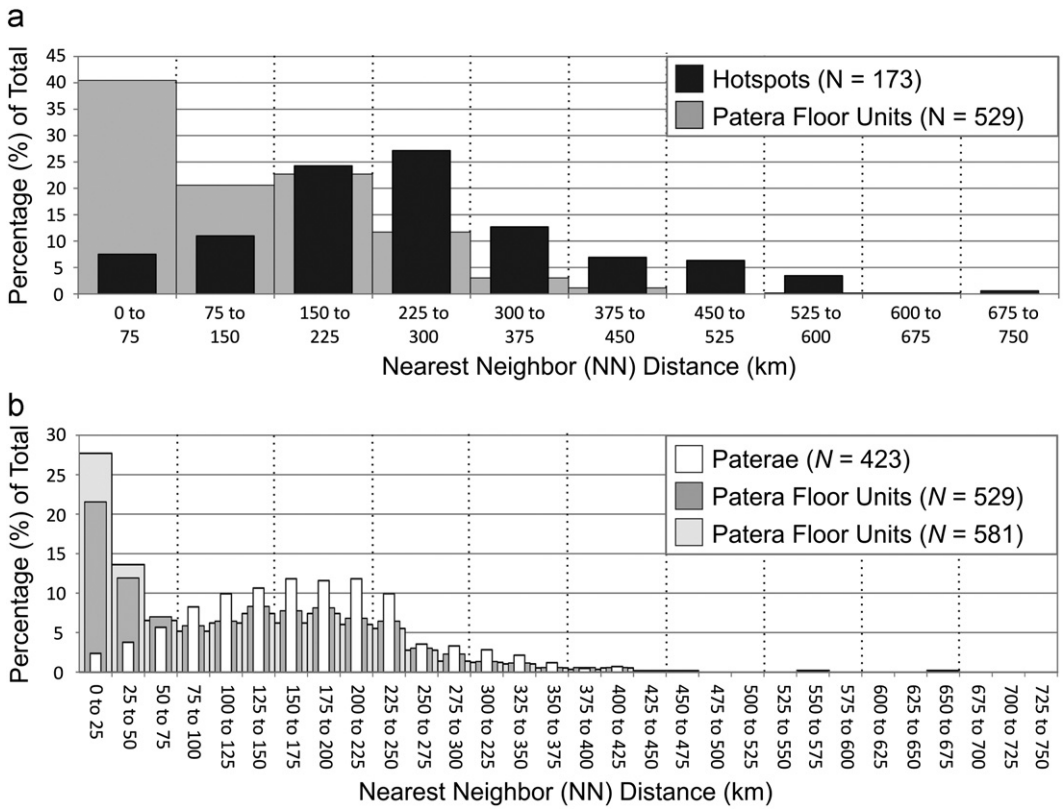

Fig. 6. Nearest neighbor (NN) distances between hotspots and paterae on Io. (a) Frequency distribution of hotspots ($N=173$) and patera floor units ($N=529$), which are the primary focus of this study. (b) Alternative patera databases compared to the $N=529$ distribution. The $N=581$ distribution is from Williams et al. (2011b) and the patera database ($N=423$) was obtained by calculating the centroids of amalgamated patera floor units ($N=581$) that are confined within topographic depressions.

whereas near-equatorial hotspots are uniform (i.e., repelled from each other) beyond 2σ levels. In general, patera floor units in the north polar, near-equatorial, and south polar regions are significantly clustered. There is an exception in the near-equatorial region, where patera floor units in the $N=529$ distribution have R and c values between their lower 1 and 2σ bound. This implies a weak, but not significant, tendency toward clustering. For the paterae distribution ($N=423$), NN distances are uniform in the south polar and near-equatorial region (beyond 2σ thresholds of significance), whereas in the north polar region they are consistent with a random model (within 1σ bounds).

In summary, hotspot locations are random on a global scale, in every hemisphere, and in the polar regions, but tend toward uniformity near the equator. In contrast, patera floor units typically exhibit clustering on global and regional scales, except in antijovian hemisphere and near-equatorial region, where patera floor units in the $N=529$ distribution are consistent with randomness. However, the implied tendency toward randomness in $N=529$ distribution may be specious given that the more recent $N=581$ database shows that patera floor units in the antijovian hemisphere and near-equatorial region are significantly clustered (beyond 2σ). Paterae—intended to represent volcanic systems rather than individual eruptive units—exhibit statistically uniformity on global and regional scales, except within the northern hemisphere and north polar regions, where their NN statistics imply randomness.

5.2. Distance-based clustering

Random NN distributions imply independent pairwise formation, but randomly-spaced pairs of points may also be organized into larger groups or clusters consisting of more than two members. We focus on the hotspot ($N=173$) and patera floor unit ($N=529$) distributions in our distance-based clustering analysis because these databases provide indicators of where volcanic activity has occurred on Io over short (decadal) and long (up to $\sim$1 million year) time scales. Only the $N=529$ patera floor unit database is analyzed here because NN results show that both the $N=529$ and 581 database are very similar on a global scale. Paterae are not included in this analysis because the database was created by dissolving the boundaries between patera floor unit that are confined within topographic depressions, and thus it may exclude overlapping volcanic systems and volcanic systems that lack a caldera-like depressions.

Distance-based clustering of volcanic centers using two cluster centers (i.e., $k=2$) identifies optimal hotspot concentrations at 17.8°S, 317.6°W and 12.7°N, 136.6°W (Fig. 7a), whereas patera floor units ($N=529$) have optimal cluster centers located at 15.6°S, 320.5°W and 1.1°N, 149.5°W (Fig. 7b).

The sensitivity analysis identified a large number of potentially significant solutions (see Supplementary material), but these near-optimal clusters concentrate within a small number of families located close to the global optima (Fig. 8). To characterize the uncertainty in cluster locations, we calculated the maximum mean cluster displacement of the potentially significant solutions from the global optimum. This uncertainty equals 120.6 km for hotspots $k=2$ (Fig. 8a), and <0.1 km for paterae $k=2$ (Fig. 8b). The fact that the near-optimal hotspot cluster centers concentrate with closely spaced families, rather than forming a degenerate set of solutions that are widely-distributed over the globe, supports the assertion that hotspots and paterae are meaningfully clustered over large regions.

For the $k=6$ hotspot solution, the coordinates of the optimum cluster centers are 41.6°N, 302.0°W; 45.6°S, 294.5°W; 9.5°N, 214.5°W; 37.0°S, 146.5°W; 28.0°N, 114.6°W; and 2.3°S, 22.0°W

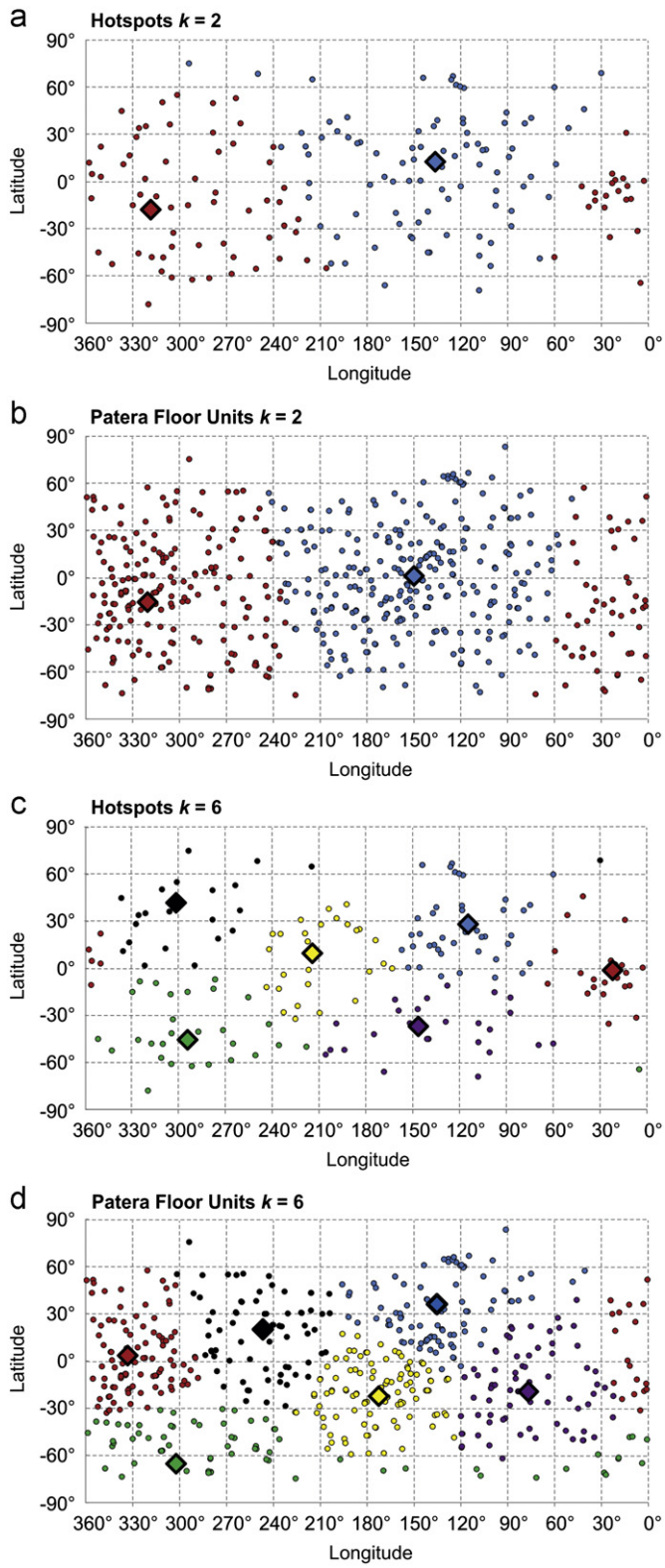

Fig. 7. Distance-based clustering results. Partitioning with two clusters ($k=2$) for (a) hotpots (N = 173) and (b) patera floor units (N = 529). Clustering results with six clusters ($k=6$) for (c) hotspots (N = 173) and (d) patera floor units (N = 529). Filled diamonds represent cluster centers and filled circles represent volcanic centers. Shared colors indicate cluster membership. The choice of $k=2$ and 6 is supported by the results of Kirchoff et al. (2011), which uses spherical harmonic analysis to demonstrate that on a global scale the only statistically significant clustering of volcanic centers (beyond 2σ) occurs at degrees 2 and 6.

(Fig. 7c). For the patera floor units ($N=529$) optimum cluster centers for the $k=6$ solution are located at: 3.0°N, 333.4°W; 65.2°S, 300.9°W; 22.8°N, 249.2°W; 22.2°S, 176.9°W; 33.5°N, 135.2°W; and 20.0°S, 77.1°W (Fig. 7d). Uncertainties in $k=6$ hotspot and patera solutions are <262 km (Fig. 8c) and <92 km (Fig. 8d), respectively. The $k=6$ hotspot centers exhibit a pattern similar to the distribution of surface heat flux maxima, but with an eastward offset of 30–60° from the tidal axis (Figs. 7 and 8c). In contrast, the $k=6$ clustering of paterae shows a pattern of cluster centers alternating between the northern and southern hemispheres (Fig. 7d). South of the antijovian point, one of the patera floor clusters shows excellent agreement with a surface heat flux maximum predicted by asthenospheric-dominated solid body tidal heating models (Fig. 8d), but in general the correspondence between cluster centers and the predicted maxima are poor.

6. Discussion: implications for tidal heating and magma ascent

6.1. Nearest neighbor analyses

We have analyzed the distribution of hotspots and paterae on Io under the assumption that hotspots represent sites of currently active volcanism, whereas patera floor units provide a longer record of Io's volcanic history spanning approximately the past 1 million years (i.e., Io's timescale of its resurfacing). However, given differences between paterae databases and the potential for observational bias due to spatially variable image resolution, we regard the volcano databases as statistical samplings, rather than a definitive inventory, and to mitigate potential sample biases we limit our NN analyses only to broad regions of Io.

On a global scale, hotspot locations are consistent with a homogeneous Poisson model, which implies that NN hotspot pairs generally form independently of one another. The same random relationship is observed among hotspots in all hemispheres. However, a different pattern emerges when hotspots in the near-equatorial regions are compared to those in near-polar regions. Hotspots in the near-polar regions of Io are randomly distributed, whereas near-equatorial hotspots exhibit a statistically significant departure from randomness (beyond 2σ) that tends toward spatial uniformity (i.e., repelling). Randomly located hotspots near the poles imply independent formation of volcanic systems at higher latitudes, perhaps suggesting a general absence of resource competition relative to the more widely-spaced hotspots near the equator. Repelling among near-equatorial hotspots suggests that pairwise interactions cause these hotspots to form at distances that are larger than would be predicted by the homogeneous Poisson model. In general, this pattern of spatial organization can be explained by a process that drives features apart in order to maximize the utilization of limited resources (Baloga et al., 2007). If Io has global asthenosphere with $\geq 20\%$ interconnected melt (Khurana et al., 2011), then there may be abundant magma at depth to drive volcanic processes, but the effects of crustal magma chambers may focus rising dikes around each volcano (Karlstrom et al., 2009). In the densely populated near-equatorial region of Io, the magma capture regions around adjacent volcanoes may lead to competition for ascending magma and contribute to larger than random NN spacing between hotspots as some volcanic systems are starved of their magma supply and new volcanic centers are inhibited from forming in close proximity to established ones. However, it is possible that other factors such as crustal heterogeneities, mountain blocks, fault distributions, and tectonic controls may also play a role in determining where magma ascends through the crust.

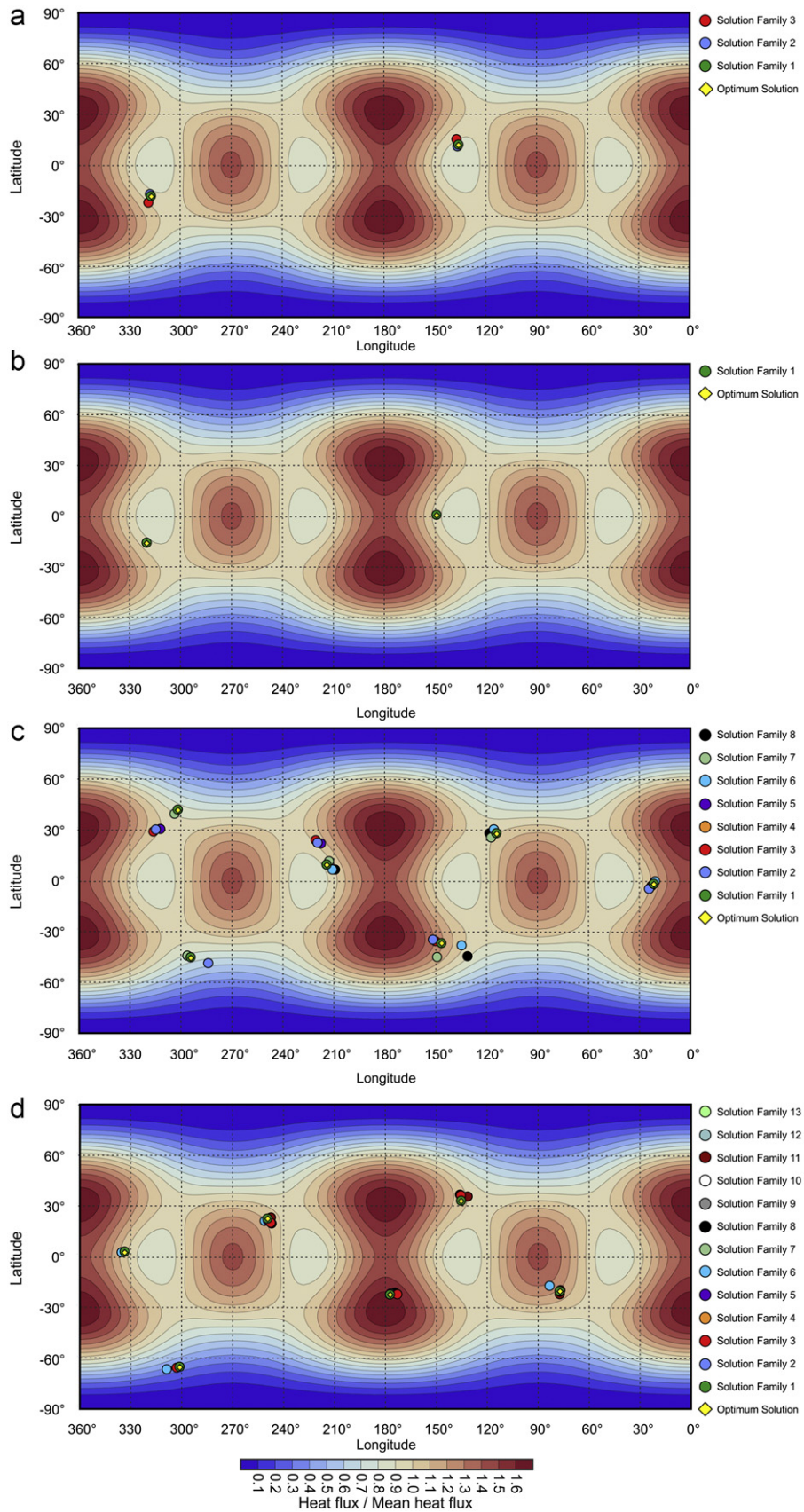

Fig. 8. Sensitivity analysis of clustering results. Near-optimum cluster center locations for (a) hotspots ($N=173$, $k=2$); (b) patera floor units ($N=529$, $k=2$); (c) hotspots ($N=173$, $k=6$); and (d) patera floor units ($N=529$, $k=6$), where k refers to the number of clusters in the analysis. Relative to the optimum solutions (yellow diamonds), the maximum mean cluster offsets among the near-optimal solutions (filled circles) are <121 km for hotspots $k=2$; <1 km for paterae $k=2$; 262 km for hotspots $k=6$; and 92 km for paterae $k=6$. Cluster centers are overplotted on the surface heat flux distribution predicted by the asthenospheric solid body tidal heating end-member (Fig. 2b).

Globally, paterae ($N=423$)—defined as caldera-like topographic depressions that may represent volcanic systems—exhibit significant repelling (beyond 2σ) between NN pairs. This implies that paterae can interact with one another to form self-organized networks with NNs spaced further apart than a homogeneous Poisson model would predict. This pattern of repelling occurs at all hemispheric and regional scales that we examined, except in northern hemisphere and north polar region, where NN distances are consistent with a random distribution. Repelling among paterae could be driven by a magma scavenging process analogous to the one proposed for controlling the spacing of active hotspots in the near-equatorial region. However, the lack of significant repelling in the northern hemisphere and north polar region may reflect independent formation of volcanic systems in these regions, or the effects of data resolution limitations at high northern latitudes.

Patera floor units—defined as bright, dark, and undifferentiated albedo units inferred to represent the products of discrete episodes of volcanic activity—exhibit global clustering within both the $N=529$ and 581 distributions. Nearest neighbor clustering of patera floor units can be attributed to the formation of multiple eruptive units in association with most volcanic systems. Hemispherically and in the near-polar regions, NN patera floor units in the $N=529$ distribution generally tend toward clustering, except in the anti-jovian hemisphere and in the near-equatorial region where they are well-described by a homogeneous Poisson model. However, using the more recent $N=581$ database, patera floor units exhibit statistically significant clustering (beyond 2σ) in all regions.

If paterae form when shallow magma chambers are partially depleted and collapse (Wood, 1984), then the presence of smaller paterae at low latitudes (Radebaugh et al., 2001; Williams et al., 2011a) implies that magma chambers at lower latitudes are smaller in size. Given that asthenospheric heating models (e.g., Tackley et al., 2001) predict that there should be ample heat available for magma generation in the equatorial regions, restrictions on crustal magma chamber sizes may result from resource competition between adjacent volcanic systems. Just as competition for magma may help to drive active hotspots away from one another, a process of dike lensing (Karlstrom et al., 2009) may favor the formation of a small number of large magma chambers that exert a strong influence on their surroundings, thereby limiting the size of other magma chambers and leading to a large number of small patera. This would explain the overall log-normal distribution of patera floor areas, which have a geometric mean of 1055 km^2 ($+2595$ km^2 and -657 km^2 at 1σ). However, even though new volcanic centers would most likely form at a maximal distance from other active volcanoes over short time periods, repeated eruption cycles could overprint the observed distribution of patera floor units and randomize it through time. This process could account for the slightly higher R values in the near-equatorial region of both the $N=529$ and 581 paterae floor unit distributions, relative to the polar regions. In contrast, patera floor units in the near-polar regions exhibit a stronger tendency toward clustering that may be explained by multiple eruptive units forming in the vicinity of longer-lived hotspots that are fed from greater depth. This is consistent with models for a thicker lithosphere in the polar region (McEwen et al., 2000a), which relative to the near-equatorial region would lead to larger, and perhaps more stable, magmatic upwellings at high latitudes (Radebaugh et al., 2001).

6.2. Frequency distributions

When considering local variations in volcano distributions on Io, it is important to account for spatial variations in image resolution (Fig. 1b). Fortunately, image coverage is generally robust between $\pm 60^\circ$ latitude (Fig. 3b). In this broad region of Io, the latitudinal population density of hotspots (Fig. 3a) is consistent with a uniform frequency distribution within 1σ confidence limits (based on χ^2 tests), whereas patera floor units have a higher population density near the equator. Note that uniformity in population density is not the same as uniformity between the NNs. The former refers to consistency in the number of volcanoes per unit area in different regions, whereas in the latter, uniformity refers to a greater than random pairwise distance relationship between volcanic centers. The uniformity of the hotspot frequency distribution may extend to higher latitudes, but given resolution limitations in the extreme polar regions, deviations from randomness are not statistically significant. The uniformity of hotspot population densities between $\pm 60^\circ$ latitude suggests that the amplitude of surface heat flux variation in this region is small. This agrees best with mixed tidal heating models that feature a significant deep-mantle component (Fig. 2c and d) and/or asthenospheric-dominated models that include surface heat flux averaging effects due to vigorous mantle convection (Fig. 2e).

The longitudinal distribution of population densities exhibits more structure with bimodal peaks in the hotspot distribution at 300–330°W and 120–150°W and in the patera distribution at 360°–330°W and 150°–180°W (Fig. 3c). The number of volcanic centers (i.e., hotspots and patera floor units) in the region from 30°W to 90°W may be slightly underestimated due to resolution limitations (Fig. 3d), but the generally strong bimodal distributions agree with asthenospheric tidal heating models that predict a dominant degree 2 pattern of volcanic activity at low latitudes near the tidal axis and at orbit tangent longitudes. Nonetheless, the longitudinal frequency distribution of volcanic centers exhibit a 30–60° eastward offset that is not explained by such models.

Correlation of the NN hotspot mode with the secondary NN mode for paterae (Fig. 4c) can be explained if multiple patera floor units tend to form in the vicinity of each hotspot, with isolated patera floor units being separated by the typical distance between NN hotspots. The primary mode among NN patera floor units may therefore provide an estimate of the length scale over which magmatic pathways branch within the volcanic systems, whereas the modal NN distance between hotspots may be used to constrain the diameter of the magma capture region surrounding major volcanic systems.

6.3. Distance-based clustering

Concentration of hotspots into two near-equatorial clusters supports a dominant role for asthenospheric heating. Within this study, $k=2$ cluster centers for hotspots and patera floor units are within a few tens of degrees of the maximum concentrations identified among patera structures by Radebaugh et al. (2001), Schenk et al. (2001), Kirchoff et al. (2011), and Veeder et al. (2011). The locations of these antipodal clusters agree with enhanced equatorial heat flux patterns predicted by asthenospheric-dominated models, but they are all offset to the east from the current tidal axis. Nonsynchronous rotation has been invoked as a possible explanation for the eastward offset of paterae from predicted surface heat flux maxima (Radebaugh et al., 2001; Schenk et al., 2001; Kirchoff et al., 2011). Alternatively, the eastward offset of volcanic concentrations from the tidal axis may be a consequence of magmatic upwelling in regions that are more favorable for magmatic ascent. For instance, if Io has a global magma ocean (Khurana et al., 2011), then magma could laterally migrate in a subsurface reservoir prior to being erupted. Regions of enhanced volcanism may therefore be related to preferred pathways to the surface rather than directly correlated with sites of maximum heat production. Note, however, that

a "magma ocean" in this context refers to an asthenosphere with interconnected partial melt and does not imply the presence of a completely fluid layer.

Anisotropies controlling the locations of magma upwelling and enhanced volcanism may include existing fault distributions in the lithosphere and the combination of stresses associated with mantle convection, magma diapirism, magma chambers, shallow intrusions, volcanic conduits, volcanic edifices, mountains, and tidal flexing (McKinnon et al., 2001; Kirchoff and McKinnon, 2009; Kirchoff et al., 2011). However, the existence of global magma ocean (Khurana et al., 2011) also raises the possibility of a fluid tidal response within this partial melt layer. Tides generated in a layer of interconnected rock melt could generate thermal energy and modify patterns of expected surface heat flux in a process that is analogous to the heating of icy satellites by fluid tidal dissipation within their liquid oceans (e.g., Tyler, 2008). The discrepancy between observed concentrations of volcanic centers and the locations of surface heat flux maxima predicted by solid body tidal heating models may therefore reflect a missing component of Io's tidal response, such as the effect of fluid tides generated within a magma ocean. Nonetheless, we cannot rule out the possibility of decoupling of volcanism from sites of maximum heat production by secondary effects such as faster than synchronous rotation and/or state of stress controls of locations of magmatic upwelling.

7. Conclusion

Differences in the spatial organization of neighboring volcanic centers in the near-equatorial and near-polar regions help to explain the complex distribution of volcanism on Io, which includes components of randomness, clustering, and uniformity. Globally, the random NN distances between hotspots suggests a smoothing of surface heat flux variations by vigorous convection and/or a deep-mantle heating component. However, the overall concentration of volcanoes at mid- to low-latitudes generally supports asthenospheric-dominated tidal heating models. On more local scales, greater than random spacing between near-equatorial hotspots implies a self-organization process that tends to drive active volcanoes apart. This process may involve the capture of ascending magma by dike lensing around each volcanic system. Such a mechanism could explain why some active hotspots appear repelled from one another and why there is a greater than random spacing between paterae, which are interpreted to be volcanic systems that have undergone one or more stages of magma chamber collapse. In contrast, patera floor units are generally clustered, which we attribute to the formation of multiple volcanic units in association with most volcanic systems.

Distance-based clustering results show a near-equatorial concentration in volcanism that is also consistent with asthenospheric-dominated tidal heating models. However, there is an unexplained 30–60° degree eastward offset in locations of volcanic centers relative to predicted surface heat flux maxima. This eastward offset may be explained by: (1) faster than synchronous rotation, (2) state of stress control on the locations of magmatic ascent from a global subsurface reservoir that decouple volcanism from sites of maximum heat production, and/or (3) a missing component of Io's tidal response, such as dissipation and heating by interconnected silicate melt within a global magma ocean.

Acknowledgments

C.W.H. is supported by an appointment to the NASA Postdoctoral Program at the Goddard Space Flight Center, administered by Oak Ridge Associated Universities through a contract with NASA. Funding for geological mapping comes to D.A.W. from the NASA Grant nos. NNG05GH43G and NNX08AQ66G. M.B. is supported by the PRODEX program managed by the European Space Agency and the Belgian Federal Science Policy Office. R.M.C.L. carried out her contribution at the Jet Propulsion Laboratory, California Institute of Technology, under contract with NASA. We thank L. Glaze, L. Kestay, L. Miller, A. Rivoldini, B. Bruno, and R. Tyler for constructive discussions, T. Hare and T. Becker for their assistance exploring the resolution of the original *Galileo-Voyager* imagery, and M. Kirchoff and an anonymous reviewer for their thorough and insightful reviews. This paper is published with the permission of the Executive Director of the British Geological Survey (NERC).

Appendix A. Supporting information

Supplementary data associated with this article can be found in the online version at http://dx.doi.org/10.1016/j.epsl.2012.10.032.

References

Baloga, S.M., Glaze, L.S., Bruno, B.C., 2007. Nearest-neighbor analysis of small features on Mars: applications to tumuli and rootless cones. J. Geophys. Res. 112, E03002, http://dx.doi.org/10.1029/2005JE002652.

Becker, T., Geissler, P., 2005. Galileo global color mosaics of Io. In: Proceedings of the Lunar and Planetary Science XXXVI. Abstract #1862. Lunar and Planetary Institute, Houston (CD-ROM).

Beggan, C., Hamilton, C.W., 2010. New image processing software for analyzing object size-frequency distribution, geometry, orientation, and spatial distribution. Comput. Geosci. 36 (4), 539–549, http://dx.doi.org/10.1016/j.cageo.2009.09.003.

Běhounková, M., Tobie, G., Choblet, G., Čadek, O., 2010. Coupling mantle convection and tidal dissipation: applications to Enceladus and Earth-like planets. J. Geophys. Res. 115, E09011, http://dx.doi.org/10.1029/2009JE003564.

Carr, M.H., McEwen, A.S., Howard, K.A., Chuang, F.C., Thomas, P., Schuster, P., Oberst, J., Neukum, G., Schubert, G., Galileo Imaging Team, 1998. Mountains and calderas on Io: Possible implications for lithosphere structure and magma generation. Icarus 135, 146–165.

Clark, P.J., Evans, F.C., 1954. Distance to nearest neighbor as a measure of spatial relationships in populations. Ecology 35, 445–453.

Geman, S., Geman, D., 1984. Stochastic relaxation, Gibbs distribution, and the Bayesian restoration of images. IEEE Trans. Pattern Anal. Mach. Intell. 6, 721–741.

Hamilton, C.W., Fagents, S.A., Thordarson, T., 2010. Explosive lava-water interactions II: self-organization processes among volcanic rootless eruption sites in the 1783–1784 Laki lava flow, Iceland. Bull. Volcanol. 72 (4), 469–485, http://dx.doi.org/10.1007/s00445-009-0331-5.

Hamilton, C.W., Fagents, S.A., Thordarson, T., 2011. Lava-ground ice interactions in Elysium Planitia, Mars: geomorphological and geospatial analysis of the Tartarus Colles cone groups. J. Geophys. Res. 116, E03004, http://dx.doi.org/10.1029/2010JE003657.

Jaeger, W.L., Turtle, E.P., Keszthelyi, L.P., Radebaugh, J., McEwen, A.S., Pappalardo, R.T., 2003. Orogenic tectonism on Io. J. Geophys. Res. 108, 5093, http://dx.doi.org/10.1029/2002JE001946.

Jaynes, E.T., 1957. Information theory and statistical mechanics. Phys. Rev. 106 (4), 620–630.

Karlstrom, L., Dufek, J., Manga, M., 2009. Organization of volcanic plumbing through magmatic lensing by magma chambers and volcanic loads. J. Geophys. Res. 114, B10204, http://dx.doi.org/10.1029/2009JB006339.

Keszthelyi, L.P., et al., 2001. Imaging of volcanic activity on Jupiter's moon Io by Galileo during the Galileo Europa Mission and the Galileo Millennium Mission. J. Geophys. Res. 106, 33025–33052.

Keszthelyi, L., Jaeger, W., Milazzo, M., Radebaugh, J., Davies, A.G., Mitchell, K.L., 2007. New estimates for Io eruption temperatures: Implications for the interior. Icarus 192, 491–503.

Khurana, K.K., Jia, X., Kivelson, M.G., Nimmo, F., Schubert, G., Russel, C.T., 2011. Evidence of a global magma ocean in Io's interior. Science 332, 1186–1189 http://dx.doi.org/10.1126/science.1201425.

Kirchoff, M.R., McKinnon, W.B., 2009. Formation of mountains on Io: variable volcanism and thermal stresses. Icarus 201, 598–614.

Kirchoff, M.R., McKinnon, W.B., Schenk, P.M., 2011. Global distribution of volcanic centers and mountains on Io: control by asthenospheric heating and implications for mountain formation. Earth Planet. Sci. Lett. 301, 22–30, http://dx.doi.org/10.1016/j.epsl.2010.11.018.

Lainey, V., Arlot, J.-E., Karatekin, Ö., Van Hoolst, T., 2009. Strong tidal dissipation in Io and Jupiter from astrometric observations. Nature 459, 957–959, http://dx.doi.org/10.1038/nature08108.
Lillesand, T.M., Kiefer, R.W., 2000. Remote Sensing and Image Interpretation, 4th ed. John Wiley & Sons, Inc., New York 724 pp.
Lloyd, S.P., 1957. Least Squares Quantization in PCM. Bell Telephone Labs Memorandum, Murray Hill, NJ. Reprinted from: IEEE Trans. Inform. Theory IT-28 2, 129-137 (1982).
Lopes-Gautier, R., The Galileo NIMS and SSI Teams, et al., 1999. Active volcanism on Io: global distribution and variations in activity. Icarus 140, 243–264, http://dx.doi.org/10.1006/icar.6129.
Lopes, R., Kamp, L.W., Smythe, W.D., Mouginis-Mark, P., Kargel, J., Radebaugh, J., Turtle, E.P., Perry, J., Williams, D.A., Carlson, R.W., Douté, S., 2004. Lava lakes on Io. Observations of Io's volcanic activity from Galileo during the 2001 Fly-bys. Icarus 169 (1), 140–174.
Lopes, R.M.C., Spencer, J.R., 2007. Io After Galileo. Springer/Praxis Publishers, Chichester, UK 342 pp.
McEwen, et al., 1998. Active volcanism on Io as seen by Galileo SSI. Icarus. 135, 181–219.
McEwen, et al., 2000a. Galileo at Io: results from high-resolution imaging. Science 288, 1198–1993.
McEwen, A.S., Lopes-Gautier, R., Keszthelyi, L., Kieffer, S.W., 2000b. Extreme volcanism on Jupiter's moon Io. In: Zimbelman, J.R., Gregg, T.K.P. (Eds.), Environmental Effects on Volcanic Eruptions: From Deep Oceans to Deep Space. Kluwer Academic/Plenum Publishers, New York, USA, pp. 179–205.
McEwen, A.S., Keszthelyi, L.P., Lopes, R., Schenk, P.M., Spencer, J.R., 2004. The lithosphere and surface of Io. In: Bagenal, F., Dowling, T., McKinnon, W. (Eds.), Jupiter: The Planet, Satellites, and Magnetosphere. Cambridge University Press, New York, USA, pp. 307–328.
McKinnon, W.B., Schenk, P.M., Dombard, A.J., 2001. Chaos on Io: a model for formation of mountain blocks by crustal heating, melting, and tilting. Geology 29, 103–106.
Moore, W.B., 2001. The thermal state of Io. Icarus 154, 548–550.
Moore, W.B., Schubert, G., Anderson, J.D., Spencer, J.R., 2007. The interior of Io. In: Lopes, J.R., Spencer, J.R. (Eds.), Io After Galileo. Praxis, Chichester, UK, pp. 89–108.
O'Reilly, T.C., Davies, G.F., 1981. Magma transport of heat on Io: a mechanism allowing a thick lithosphere. Geophys. Res. Lett. 8, 313–316.
Peale, S.J., Cassen, P.R., 1978. Contribution of tidal dissipation to lunar thermal history. Icarus 36, 245–269.
Peale, S.J., Cassen, P.R., Reynolds, T., 1979. Melting of Io by tidal dissipation. Science 203 (4383), 892–894.
Radebaugh, J., Keszthelyi, L.P., McEwen, A.S., Turtle, E.P., Jaeger, W., Milazzo, M., 2001. Paterae on Io: a new type of volcanic caldera? J. Geophys. Res. 106, 33005–33020.
Rathbun, J.A., Spencer, J.R., Davies, A.G., Howell, R.R., Wilson, L., 2002. Loki: a periodic volcano. Geophys. Res. Lett. 29 (10), 1443, http://dx.doi.org/10.1029/2002GL014747.
Roberts, J.H., Nimmo, F., 2008. Tidal heating and the long-term stability of a subsurface ocean on Enceladus. Icarus 194, 675–689.
Rose, K., 1998. Deterministic annealing for clustering, compression, classification, regression, and related optimization problems. Proc. IEEE 86 (11), 2210–2239.
Ross, M.N., Schubert, G., Spohn, T., Gaskell, R.W., 1990. Internal structure of Io and the global distribution of its topography. Icarus 85, 309–325.
Ross, M.N., Schubert, G., 1985. Tidally forced viscous heating in a partially molten Io. Icarus 64, 391–400.
Sabadini, R., Vermeersen, B., 2004. Global Dynamics of the Earth: Applications of Normal Mode Relaxation Theory to Solid-Earth Geophysics. Kluwer Academic Publishers, Dordrecht.
Schenk, P.M., Hargitai, H., Wilson, R., McEwen, A., Thomas, P., 2001. The mountains of Io: global and geological perspectives from Voyager and Galileo. J. Geophys. Res. 106, 33201–33222.
Schubert, G.T., Spohn, T., Reynolds, R.T., 1986. Thermal histories, compositions and internal structures of the moons of the solar system. In: Burns, J.A., Matthews, M.S. (Eds.), Satellites. University of Arizona Press, Tucson, USA, pp. 224–292.
Segatz, M., Spohn, T., Ross, M.N., Schubert, G., 1988. Tidal dissipation, surface heat flow, and figure of viscoelastic models of Io. Icarus 75, 187–206.
Shannon, C.E., 1948. A mathematical theory of communication. Bell Syst. Tech. J. 27 (379–423), 623–656.
Smith, et al., 1979a. The Galilean satellites and Jupiter-Voyager 2 imaging science results. Science 206, 927–950.
Smith, et al., 1979b. The Jupiter system through the eyes of Voyager 1. Science 204, 951–972.
Spencer, et al., 2007. Io volcanism seen by New Horizons. Science 318, 240–243, http://dx.doi.org/10.1126/science.1147621.
Spencer, J.R., Rathbun, J.A., Travis, L.D., Tamppari, L.K., Barnard, L., Martin, T.Z., McEwen, A.S., 2000. Io's thermal emission from the Galileo photopolarimeter-radiometer. Science 288, 1198–1201.
Spohn, T., 1997. Tides of Io. In: Wilhelm, H., Zurn, W., Wenzel, H.G. (Eds.), Tidal Phenomena, Lecture Notes in Earth Sciences, vol. 66. Springer Verlag, Heidelberg, pp. 345–377.
Tackley, P.J., Schubert, G., Schenk, P., Ratcliff, J.T., Matas, J.-P., 2001. Three-dimensional simulations of mantle convection in Io. Icarus 149, 79–93, http://dx.doi.org/10.1006/icar.2000.6536.
Tackley, P.J., 2001. Convection in Io's asthenosphere: redistribution of nonuniform tidal heating by mean flows. J. Geophys. Res. 106 (E12), 32,971–32,981.
Tyler, R.H., 2008. Strong ocean tidal flow and heating on moons of the outer planets. Nature 456 (11), 770–772, http://dx.doi.org/10.1038/nature07571.
Turcotte, D.L., Schubert, G., 2002. Geodynamics, 2nd ed. John Wiley & Sons, New York, USA 456 pp.
Tobie, G., Mocquet, A., Sotin, C., 2005. Tidal dissipation within large icy satellites: applications to Europa and Titan. Icarus 177, 534–549, http://dx.doi.org/10.1016/j.icarus.2005.04.006.
Turtle, E.P., et al., 2004. The final Galileo SSI observations of Io: orbits G28-I33. Icarus 169, 3–28.
Turtle, E.P., Jaeger, W.L., Schenk, P.M., 2007. Ionian mountains and tectonics: insights into what lies beneath Io's lofty peaks. In: Lopes, R.M.C., Spencer, J.R. (Eds.), Io After Galileo. Praxis, Chichester, UK, pp. 109–131.
Veeder, G.J., Davies, A.G., Matson, D.L., Johnson, T.V., 2009. Io: Heat flow from dark volcanic fields. Icarus 204, 239–253, http://dx.doi.org/10.1016/j.icarus.2009.06.027.
Veeder, G.J., Davies, A.G., Williams, D.A., Matson, D.L., Johnson, T.V., Radebaugh, J., 2011. Io: Heat flow from dark paterae. Icarus 212, 236–261, http://dx.doi.org/10.1016/j.icarus.2010.09.026.
Veeder, G.J., Davies, A.G., Matson, D.L., Johnson, T.V., Williams, D.A., Radebaugh, J., 2012. Io: volcanic thermal sources and global heat flow. Icarus 219, 701–722 http://dx.doi.org/10.1016/j.icarus.2012.04.004.
Williams, D.A., Radebaugh, J., Keszthelyi, L.P., McEwen, A.S., Lopes, R.M.C., Douté, S., Greeley, R., 2002. Geologic mapping of the Chaac-Camaxtli region of Io from Galileo imaging data. J. Geophys. Res., 107 (E9), 5068, http://dx.doi.org/10.1029/2001JE001821.
Williams, D.A., Keszthelyi, L.P., Crown, D.A., Yff, J.A., Jaeger, W.L., Schenk, P.M., Geissler, P.E., Becker, T.L., 2011a. Volcanism on Io: new insights from global geologic mapping. Icarus 214, 91–112, http://dx.doi.org/10.1016/j.icarus.2011.05.007.
Williams, D.A., Keszthelyi, L.P., Crown, D.A., Yff, J.A., Jaeger, W.L., Schenk, P.M., Geissler, P.E., Becker, T.L., 2011b. US Geological Survey Scientific Investigations Map 3168. Scale 1:15,000,000, 25 p. 〈http://pubs.usgs.gov/sim/3168/〉.
Wood, C.A., 1984. Calderas: a planetary perspective. J. Geophys. Res. 89, 8391–8406.